Supplementary Information (SI) for Soft Matter.
This journal is © The Royal Society of Chemistry 2025

Supporting Information for: Mechanism of Microplastic and Nanoplastic Emission from Tire Wear

Shankar Ghosh,*[a] Anit Sane,[a], Smita Gohil,[a] Vedant Vashishtha,[b] Sanat K. Kumar *[c] and Guruswamy Kumaraswamy*[b]

1 Materials and Methods

1.1 Experimental setup:

The experimental setup is schematically represented in Fig. 1 (in the main manuscript) . Two electric brushless hub motors were arranged vertically on a rigid metal frame. We mount a Michelin 90/100 tire on the top electric motor. The top electric hub motor was driven by a controller that was powered by a regulated 48V and 30 A power supply, allowing us to rotate the tire. The outer diameter, $2R_{\text{tire}}$, of the tire is 430 mm and the width of the tire is 180 mm (Fig. S1(b)). The axle of this motor is mounted on a 200 kg load cell (Fig. S1(d)). This allowed us to measure the normal force, F_N, acting on the tire as it contacts the (bottom drum) "pavement". The load cell is powered by 12 V and its output voltage is measured using a Keithley Multimeter 2000. Typical change in voltage for this load cell is 0.1 mV/kg. Tire pressure was maintained at 250kPa (36 psi) during all experiments. The lower electric motor had an aluminum cylinder with an outer diameter $2R_{\text{drum}}$ of 280 mm and thickness of 3 mm welded to it as can be seen in Fig. S1(c). This cylinder was cut with 1 mm deep groves that ran both parallel and perpendicular to its axis. The grooves that ran along the circular circumference of the cylinder were machined to be 3 mm apart, while those that ran parallel to the axis were spaced 10 cm apart (Fig.S1(e)). These numbers were chosen with the aim of mimicking typical tining of a concrete road[1,2]. We confirmed that the metal cylinder does not wear out during the experiment, so that the wear particles observed come only from the tire. The electric motor on the bottom was not powered and therefore was free to rotate. The vertical position of the bottom motor can be varied. In our experiments, it is adjusted such that the aluminium cylinder that mimics the pavement contacts and presses against the tire. We control the normal load for the tire-pavement contact by changing the distance between the top and the bottom electric hub motors (Fig.S1(e)).

1.2 Experimental protocol:

The entire system is placed inside a plexiglass chamber whose dimensions are given in Fig. S1(a)). Experiments are conducted as follows. Before the start of measurements, the enclosure is continuously flushed with filtered air for several hours. During the entire flushing process, particle counts are monitored. The typical ambient conditions in the laboratory are such that the 0.3 μm channel of the particle counter typically registers a value of 10000 counts, at the start of the flushing operation. As we flush the chamber, this number decreases and we continue pumping filtered air until this channel records a count of the order of few 100. This process of cleaning the chamber typically takes a few hours. Once this baseline count value is reached, the valves are closed and the flushing is stopped. We have confirmed that, once the chamber is isolated after the end of the flushing operation, particle counts did not change significantly over a period of several hours. This cleaning operation was conducted before the start of every experiment.

Tire wear experiments commence after cleaning the enclosure, by powering on the top motor that the tire is mounted on. A constant regulating voltage was applied to the controller to ensure that the tire operates at a given speed. Under our experimental conditions, it typically takes about 10 seconds for the tire to reach its desired value. We monitor the rotation speed ω_{tire} of the tire and the aluminium drum ω_{drum} using an inductive sensor whose output is fed to an oscilloscope, as well as using a non contact digital tachometer. We also monitor the normal load using a load cell mounted on the axle of the top motor. The linear velocity of the tire is given by $v = \omega_{\text{tire}} R_{\text{tire}}$. The experiment continues for at most 10 minutes, after which the motor is powered off. At lower velocities and normal loads, where tire wear particles are emitted at a lower rate, we collect samples for 10 minutes. For higher v and F_N, we collect samples for a shorter time, but never less than 5 minutes. Wear particles emitted by the tire that are aerosolized are measured using the particle counter. As an example, we present data obtained in a typical experiment in Fig. S5. At the start of the experiment, before the tire is powered on, we observe a low baseline value for the particle counts.

[a] *DCMP&MS, Tata Institute of Fundamental Research,* Homi Bhabha Road, Mumbai, 400005, Maharashtra, India. ; E-mail:sghosh@tifr.res.in
[b] *Department of Chemical Engineering, Indian Institute of Bombay, Mumbai, India. 400076 ; E-mail:guruswamy@iitb.ac.in*
[c] *Department of Chemical Engineering, Columbia University,* 500 W 120th St, New York City, USA; E-mail:sk2794@columbia.edu

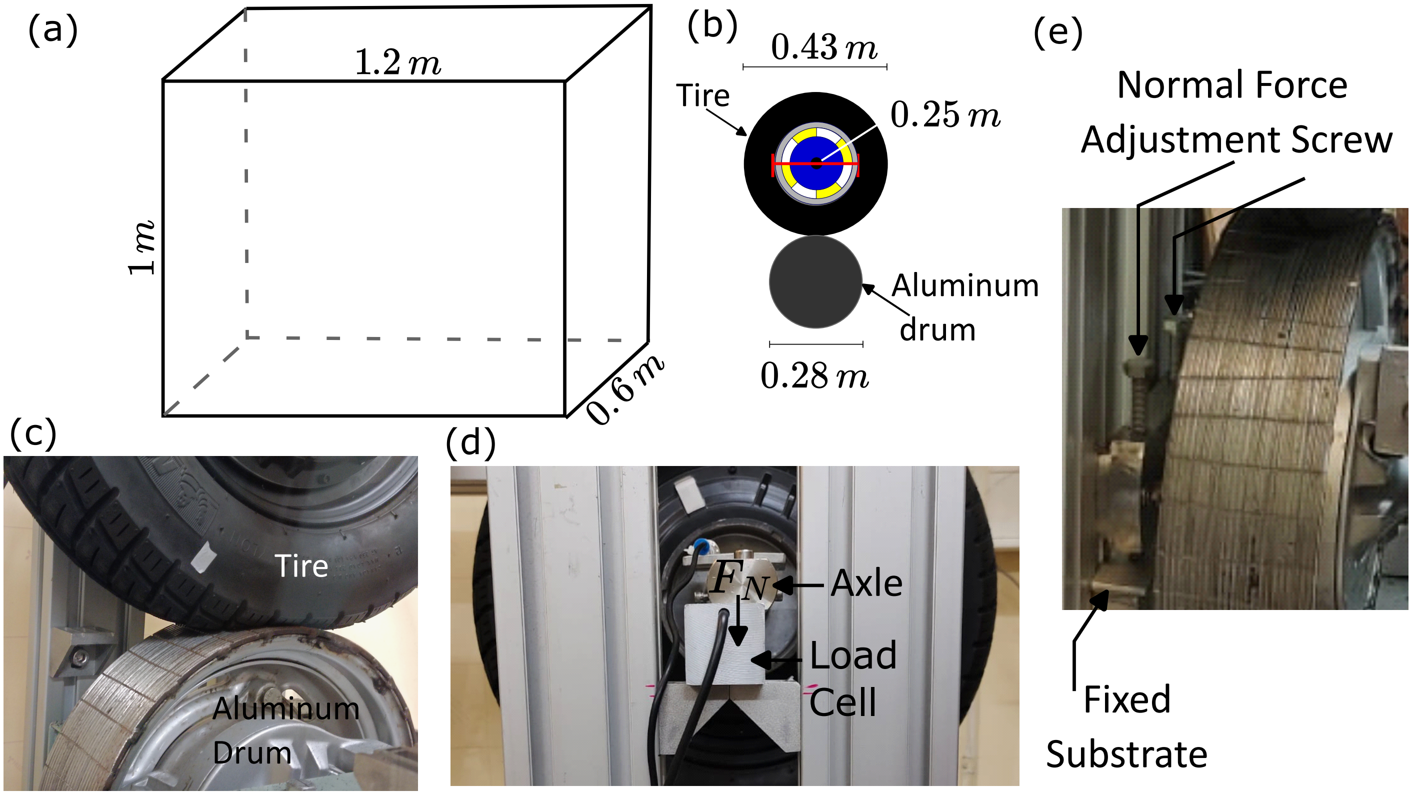

Fig. S1 (a) and (b) show the dimensions of the enclosure, the tire and the rollers in meters. In (c) we show a photograph of the contact between the tire and the bottom roller. (d) Shows the axle and load cell configuration, where the load cell measures the normal force F_N. (e) Shows the arrangement that we use to adjust the normal force. When the screws shown in the image are adjusted, the bottom roller is raised while maintaining the tire height, which increases the normal force F_N.

1.3 Heating up of the tires:

As the tire runs against the aluminium drum, it heats up. We monitor the tire temperature during the experiment using an IR sensor from RAYTEK, with the sensor mounting shown in Fig. S2. Representative time plots showing the temperature evolution of the tire for different values of v at $F_N = 700$N are presented in Fig. S2(b). We observe a moderate increase in the tire's saturation temperature T_{sat} above ambient levels as it begins to rotate. Our experimental conditions were chosen to ensure that the increase in tire temperature does not exceed 20°C above ambient during the period when tire wear particles were collected, even under the highest loads and rotation speeds. The maximum temperature observed for each experimental condition is summarized in Table 1.

1.4 Scanning electron micrographs of MNPs:

Figure S3 presents scanning electron micrographs of tire wear MNPs . Panel (a) displays a representative image of an aerosolized particle. These MNPs were collected from the region near the particle counter (near the top of the enclosure). Panels (b) and (c) show images of MNPs deposited on the LED imaging plate (near the bottom of the enclosure). Energy dispersive x ray spectroscopy analysis from a spot on the MNP indicates that the MNPs consist primarily of about 85% carbon, 10% oxygen, and trace amounts of silicon, sulphur, calcium, iron, and zinc.

	7 km/h	12 km/h	17 km/h	22 km/h	27 km/h	31 km/h
90N	25°C	25.9°C	27°C	27.7°C	29°C	29.4°C
230N	26.4°C	27.1°C	29.6°C	30°C	35°C	37 °C
300N	29.5°C	33°C	35.4°C	37.4°C	38.1 °C	40.8 °C
400N	28.9°C	32.9°C	38.4°C	40.7°C	42.2°C	42.6 °C
540N	29.8°C	35.3°C	38°C	41.7°C	42.4 °C	47.7 °C
700N	34.2°C	36.7°C	41.8°C	43.6°C	46.9 °C	49.1 °C

Table 1 The maximum saturation temperatures T_{sat} for experiments at different v and F_N.

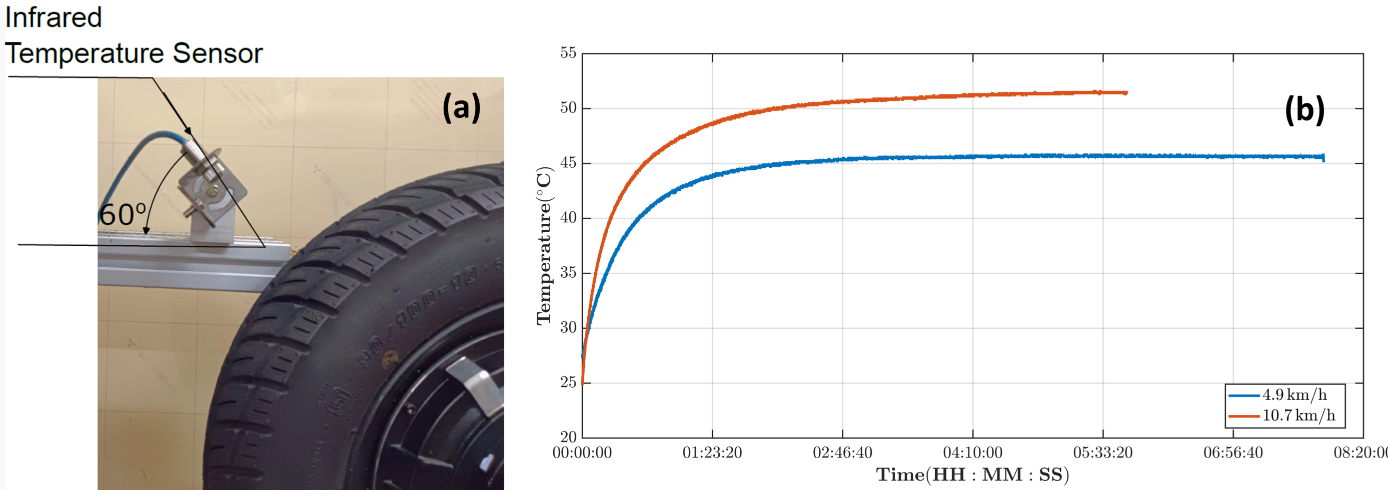

Fig. S2 (a) The photograph displays the installation of the infrared temperature sensor, which is used to measure the tire's temperature. (b) The time evolution of the temperature of the tire for representative values of v for $F_N = 700N$. The tyre is set to motion at $t = 0$ s.

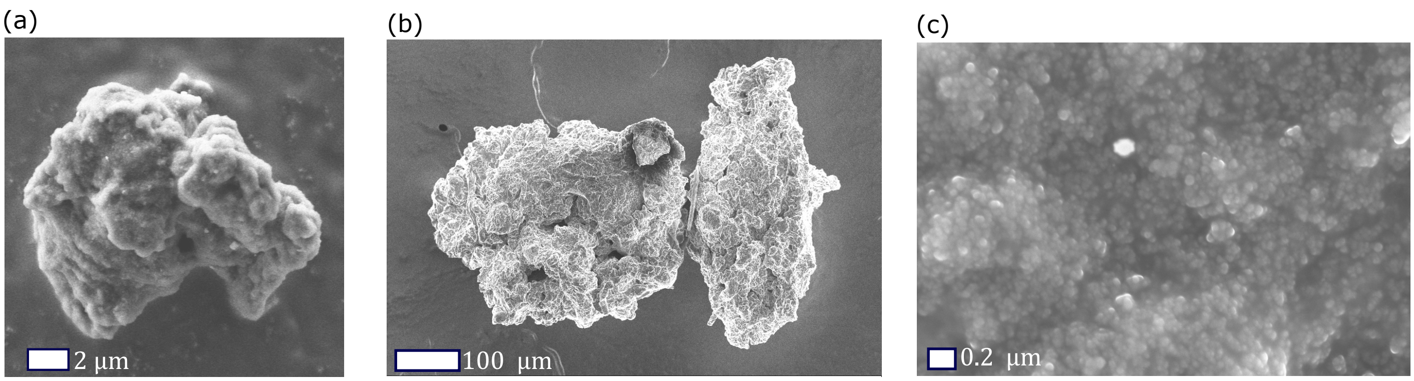

Fig. S3 The scanning electron micrographs show (a) a region near the particle counter and (b, c) MNPs on the imaging plate.

1.5 Counting the worn out MNPs :

Tire wear MNPs emitted during the experiments are characterized (i) by using a DSLR camera to image MNPs deposited on a LED panel, as shown in the schematic (Fig.1, main manuscript) and (ii) using an aerosol particle counter (SPC 8000 particle counter manufactured by Setra). We note that this protocol provides us with an *in situ* estimate of all the emitted particles, allowing us to “stitch" together the data from these two techniques over length scales ranging over 5 orders, from 300 nm to ≈10 mm. However, experimental limitations exclude data over a decade, from 10μ to 0.1 mm. While techniques such as microscopy can be used to provide data in this missing range, these are *ex situ* techniques that would examine a limited sample size. Therefore, we limit ourselves to reporting data using the aerosol counter and DSLR imaging.

Imaging by DLSR camera : This method of imaging was limited mainly to MNPs that are about 0.1 mm or larger in diameter. The image is first processed by subtracting the background and then applying a threshold. The resulting thresholded image consists of regions of connected clusters of pixels, each region representing a distinct particle. The properties like diameter and shape (eccentricity, see below) of these clusters (MNPs) were then computed. For anisotropic particles, we use the largest dimension as the particle diameter. In the left panel of Fig. S4 we plot the variation of the number of MNPs per second collected on the imaging plate as a function of the velocity and normal force. The number of these MNPs increases with both tire velocity v and normal force F_N.

Shape of tire wear MNPs: The MNPs are often oblong. To characterise this we measured the variation in eccentricity (ε) of the MNPs imaged by the DSLR camera as a function of tire velocity v and normal force F_N. For each connected cluster (particle), the second moment is calculated, and an ellipse with matching second moments is associated with it. The variation of the average eccentricity of these corresponding ellipses as a function of the control parameters (v and F_N) is what is depicted in the right panel of Fig. S4. The MNPs were found to become substantially more elliptical with increasing velocity v and normal force F_N. The maximum value of the eccentricity, obtained at the highest normal loads and speeds, was ≈ 0.5 - 0.6, corresponding to particles with an aspect ratio of ≈ 1.2.

Counting by the aerosol particle counter : This portable model (SPC 8000 particle counter manufactured by Setra) has a flow rate of 2.83 lpm and has six size channels that are set at 0.3, 0.5, 1, 2.5, 5 and 10 μm. We confirmed that there was no difference in the readings obtained when we mounted the aerosol counter at different locations within the experimental enclosure. For the measurements

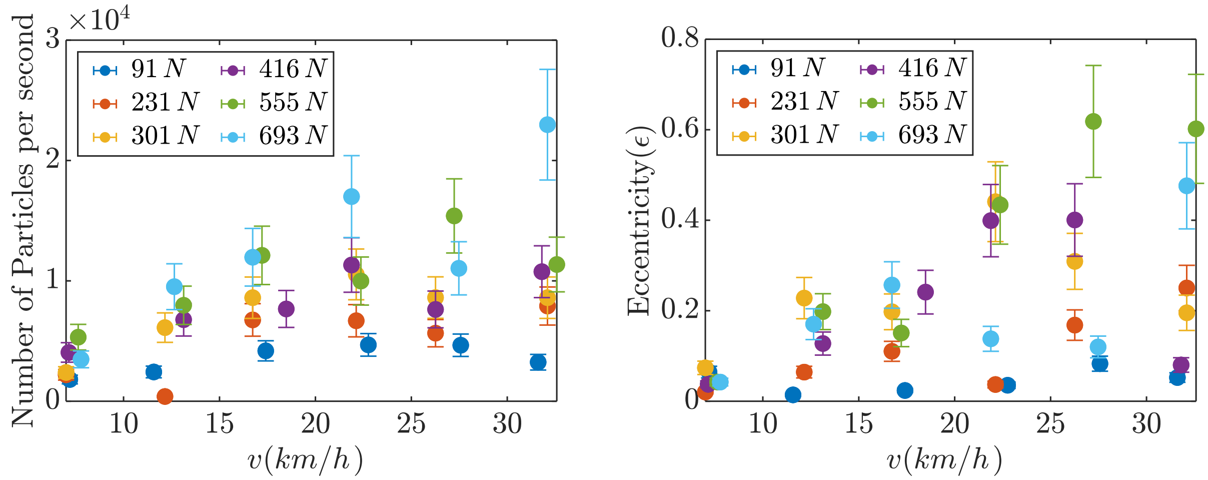

Fig. S4 Left panel : Variation of the total number of MNPs (particles per second) collected on the imaging plate as a function of the velocity and normal force. Right Panel: The plot illustrates the variation in eccentricity (ε) as a function of tire velocity v and normal force F_N, of the MNPs captured by the DSLR camera.

reported here, the location of the particle counter is as shown in the schematic (Fig. 1, main manuscript). We obtain the total MNPs at each size channel from the experimentally measured particle generation rate, multiplied by the tire run time and the enclosure volume.

Once the tire starts rotating, there is an immediate increase in the counts measured (Fig. S5). This increase in count rate is sublinear over the 10 minutes time scale for which the tire is run. Sublinear growth arises from the operation of the particle counter that employs a constant flow rate of 2.83 lpm for sampling. This stream is filtered as it is returned leading to the observed sublinear increase. During this phase, the increase in particle counts for each channel is well modelled using the functional expression $n_c = n_c^0(1 - exp(-t/\tau))$. We note that this form is empirical and has no theoretical basis - it was chosen simply because it fit the data well. Thus n_c^0/τ is a measure of the rate at which MNPs are generated for that channel. We represent this as $\partial_t n(d)$, the rate at which MNPs with a size, d are generated.

The power to the tire motor is turned off at the end of the experiment (marked "Off" in Fig. S5) , after which the particle counts decrease. Once the tire stops rotating, no new wear MNPs are generated. The decrease in particle counts in the enclosed chamber after cessation of tire rotation arises due to a combination of three factors: (i) air sampled by the aerosol counter passes through a filter that reduces the suspended particle count (discussed previously, in the context of the sublinear increase in particle counts with time when the tire is powered on), (ii) sedimentation of MNPs , and (iii) electrostatic adsorption of MNPs onto the side walls of the enclosure.

1.6 Stitching of the data from the particle counter and imaging

The particle counter provides real-time measurements of MNPs within the sampled volume. Over time, this value increases, initially in an almost linear fashion.To estimate the number of MNPs $\partial_t N_d^{pc}$ in the enclosure per channel of measurement, per unit time, we calculate the slope of the initial growth phase from the particle counter's measurements for each channel (see Fig. S5) and multiply it with the volume of the container ($\sim 0.72 m^3$). For the imaging using the DSLR camera, we directly use the histogram values of the MNPs per unit time obtained from imaging, $\partial_t N_d^{DSLR}$.

Thus the function $\partial_t N_d$ describes the number of MNPs per unit time across the two methods of detection

$$\partial_t N(d) = \begin{cases} \partial_t N_d^{pc} & \text{if } d \leq 0.01\,\text{mm}, \\ \partial_t N_d^{DSLR} & \text{if } d \geq 0.1\,\text{mm} \end{cases}$$

By taking the probability density function of N_d we compute $\partial_t n(d)$ (see Fig. 2, main manuscript). By definition, the area under the probability density function is unity. The data$\partial_t n(d)$ fit well with the functional expression $\partial_t n(d) = \frac{A}{d^\alpha}\exp(-\frac{d}{d_o}) + \frac{B}{d\sigma\sqrt{(2\pi)}} exp(\frac{(ln\frac{d}{\mu})^2}{2\sigma^2})$, where d_o is associated with the exponential cutoff, and α is the power-law exponent. The function is constructed to fit the data with the constraint that the area under the pdf is unity. While the variation of the other parameters is discussed in the main text, in Fig. S6 we plot the variation of the σ and μ as a function of velocity and normal force F_N.

1.7 Experiments with a different "pavement":

To examine the role of pavement-tire interactions on the size distribution of the larger tire wear microplastics, we performed experiments using the same tire that was run against a different roller as shown in Fig.S7 (a),(b). Here, the roller is a metal cylinder cut with 0.5 mm grooves, finer. We image the large microplastic fragments that are deposited and analyze their particle size distribution (Fig. S7 c).

We observe that the particle size distribution has shifted to smaller sizes relative to Fig. 2 (in the main manuscript). This is consistent with the reduction in the groove size of the roller relative to that employed to generate Fig. 2 (main manuscript). The shape of the size distribution is consistent with a log-normal distribution - however, it is difficult to fit this data reliably since the peak of the distribution is not accessible through our imaging measurements.

1.8 Charge measurement:

We used a Keithley 6514 electrometer to measure the net charge Q carried by the worn out tire MNPs. We positioned a stainless steel metal plate 60×30 cm^2 to collect the deposited MNPs, as shown in the Fig. 1 (c) (main manuscript). This metal plate was electrically isolated from the ground using insulating posts. The input of the electrometer is a three-lug triax connector, with the innermost wire (input high) being the charge sensing terminal. This charge sensing terminal of the electrometer was connected to the metal plate. In our experiments, we used the guard-off condition, i.e., the common (input low) and the chassis are grounded. After each experiment, the weight M of the worn out MNPs deposited on the plate was measured. The time trace of the charge recorded by the electrometer before, during and after the motion of the tire is plotted in the inset of Fig.S8. The 'ON' and 'OFF' time instances marked in the inset figure indicate the switching on and off of the power to the tire. One notes that the tire wear MNPs have a net negative charge. The charge per unit mass Q/M generated per unit time increases as a function of the velocity, this is shown in Fig. S8. However, this ratio does not depend on F_N. The triboelectric charging of particles of different size is a well studied topic, and it is known that the small and large particle sizes in a distribution of sizes acquire opposite charge[3]. More work is needed to characterize the charge of the large sized particles to develop a full understanding of this topic.

1.9 Dissipation and power consumption:

As the tire runs against the aluminum drum, it begins to slip. The slip velocity $\delta v = \omega_{\text{tire}} R_{\text{tire}} - \omega_{\text{drum}} R_{\text{drum}}$ is measured as a function of the linear velocity of the tire $v = \omega_{\text{tire}} R_{\text{tire}}$ for various values of the normal load F_N. Figure S9 (a) shows the linear variation of the slip velocity δv as a function of the velocity v for different values of the normal force F_N. The solid lines in the plot represent linear fits to the data. The inset to Fig. S9 (a) displays the variation of the slope of these fits, $\delta v/v$, as a function of F_N, showing that $\delta v/v \sim \sqrt{F_N}$.

The slipping of the tire against the cylindrical drum causes increased traction and frictional dissipation. A part of this dissipated heat is converted to heat and the rest is used up in the process of wearing. The contribution to heat is tabulated in Table 1. Moreover, the specific surface area of the particles were also shown to scale with the product of the velocity v of the tire and the normal force F_N (see Fig. 3 (b), main manuscript). In principle, one could add all these sources of dissipation, however, this is difficult to do quantitatively. Instead, we study the power consumed by the hub motor as a function of slip velocity δv and normal force F_N.

The hub motor is powered by a 48V power source and its RPM is adjusted by appropriately modifying the pulse timing of the controller. We measure the electrical power P consumed by the central motor by monitoring the RMS current I_{rms} it draws, where $P = 48I$, using a general purpose multimeter. As the RPM increases, the tire consumes more electrical power, and since the slip velocity is directly proportional to the RPM, the power consumed varies linearly with δv. This linear relationship is depicted in Fig. S9(b). The solid lines indicate linear fits.

The traction force behaves similarly to Coulomb friction, where the magnitude of the tractive force is proportional to the normal force F_N. Therefore, it is reasonable to expect that the power consumed by the motor would increase with F_N. However, inset of Fig. S9 (b) reveals the non-monotonic variation of the slope of these fits, $P/\delta v$, as a function of F_N. This would suggest that worn-out particles behave as a lubricant on dry surfaces.

Notes and references

1 M. B. Snyder *et al.*, *Concrete Pavement Texturing*, United states. federal highway administration. https://www.fhwa.dot.gov/pavement/pubs/hif17011.pdf technical report, 2019.

2 *The Standard Specifications for the Construction of Roads and Bridges on Federal Highway Projects*, US Dept. of Transportation; https://highways.dot.gov/federal-lands/specs: :text=Standard.

3 D. J. Lacks, N. Duff and S. K. Kumar, *Phys. Rev. Lett.*, 2008, **100**, 188305.

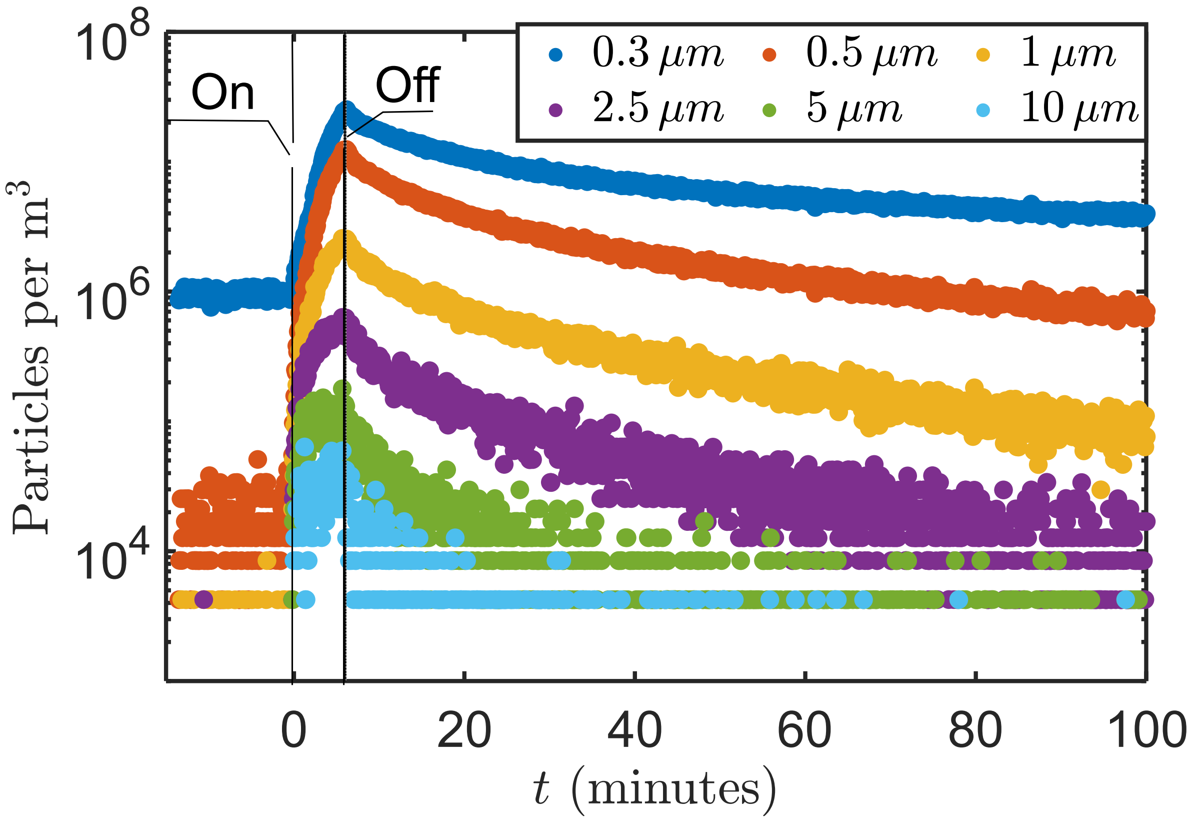

Fig. S5 (a) Time trace of the counts from the various particle channels of the counter, prior to, during and after the motion of the tire. The 'On' and 'Off' time instances marked on the figure indicates the switching on and off of the power to the tire.

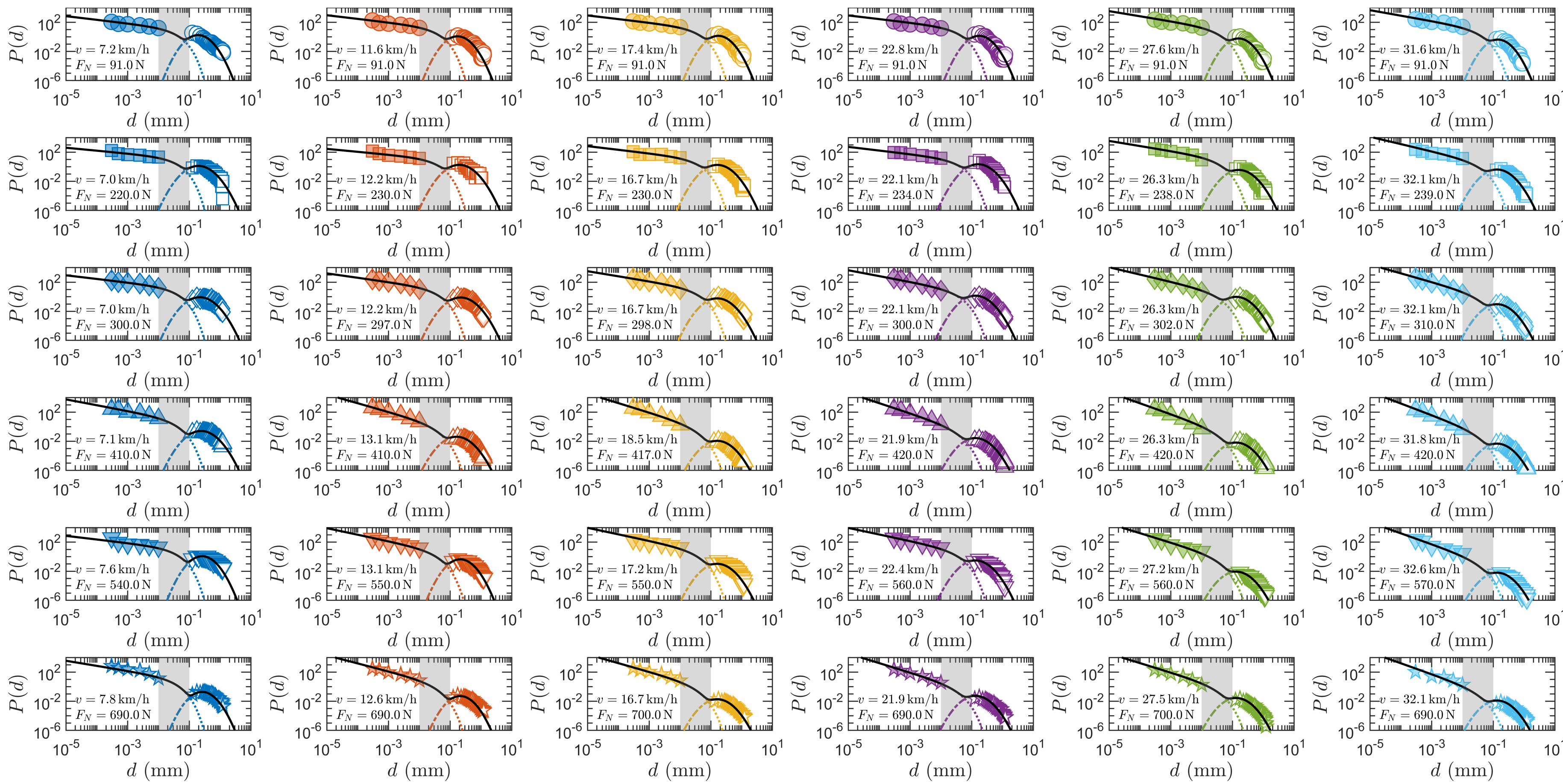

Fig. S5 (b) The probability density function (pdf) for the particles generated is plotted for different values of the normal force F_N and v. Filled symbols denote data from the particle counter, while open symbols illustrate data from imaging experiments. Fits to the data using the two-part expression described in the main manuscript are shown.

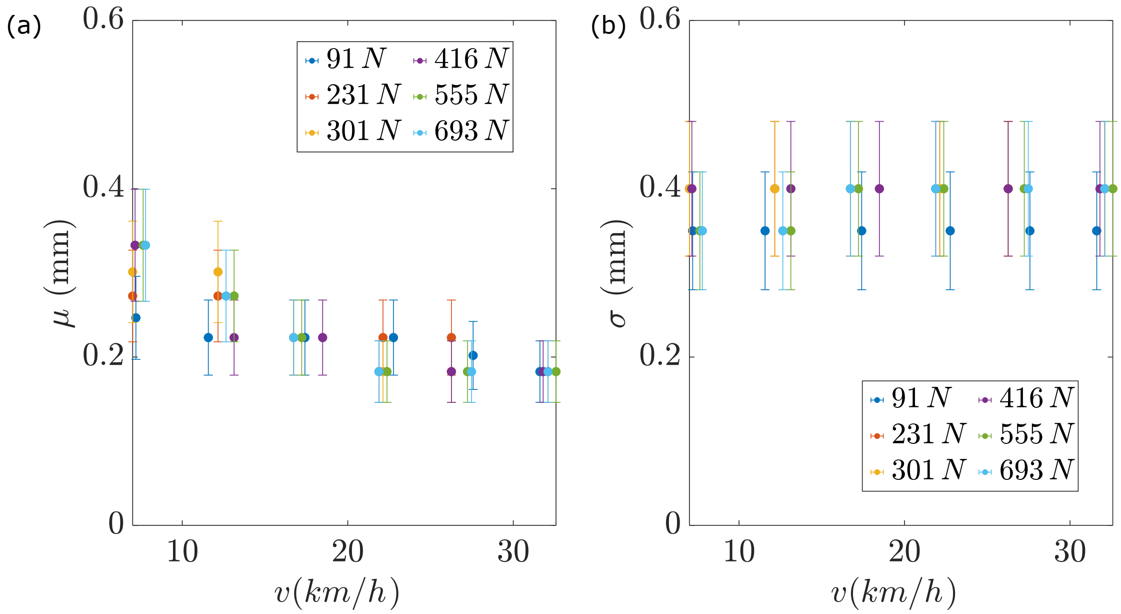

Fig. S6 Plot showing the variation of fitting parameters, μ and σ, as a function of velocity and normal force F_N

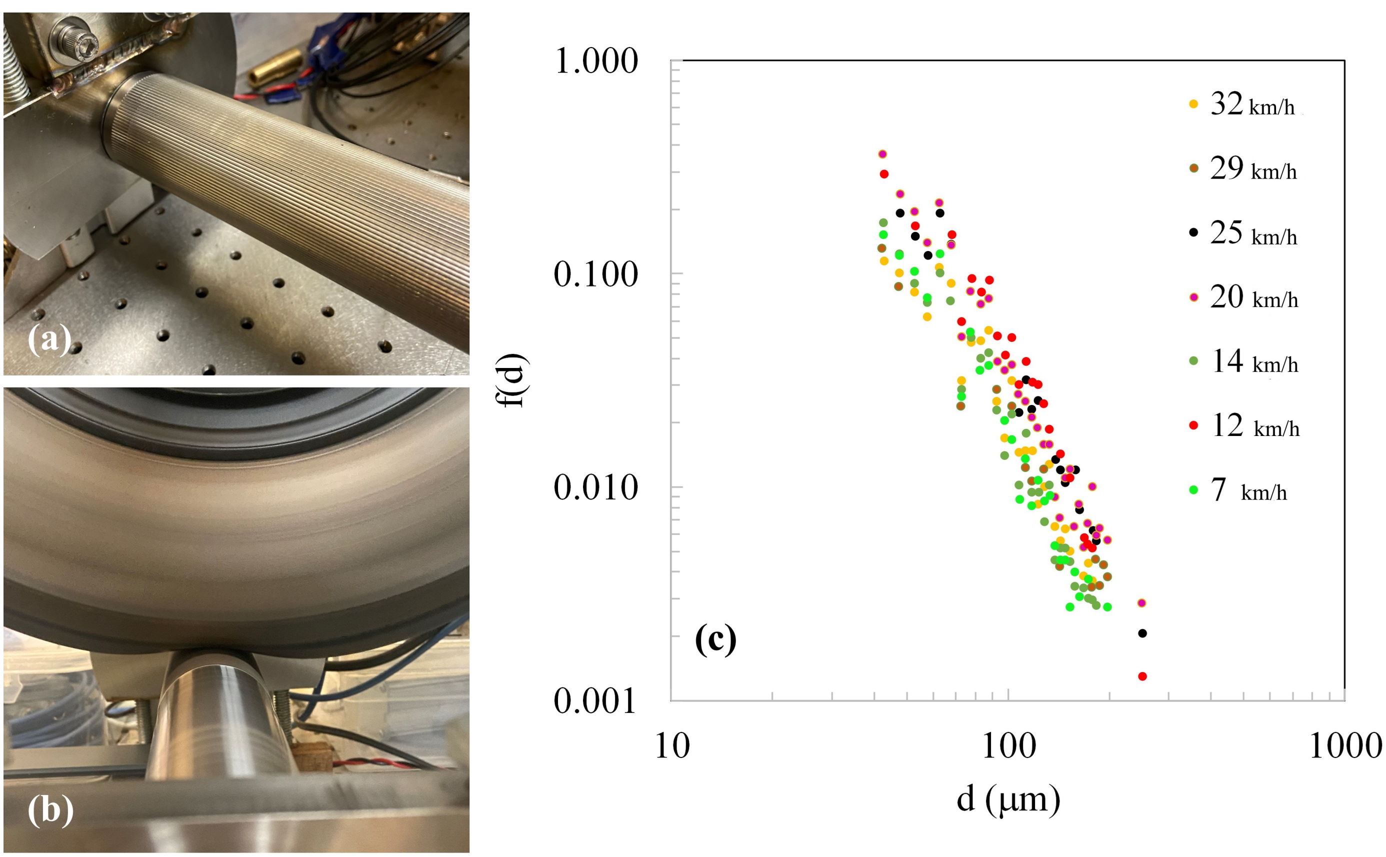

Fig. S7 (a) Metal roller cut with 0.5 mm deep grooves (compare with the 1 mm deep grooves cut to mimic tining of concrete roads in Fig. S1 e). (b) The tire runs against the bottom roller and tire wear particles formed are imaged using a camera. The tire is inflated to the same pressure in all experiments reported here and the normal load is fixed at 294 N. (c) Size distribution for the tire wear particles generated, imaged using the camera. Only particles larger than $\sim 30\mu$m can be detected. f(d) represents the (binned) fraction of particles with size d.

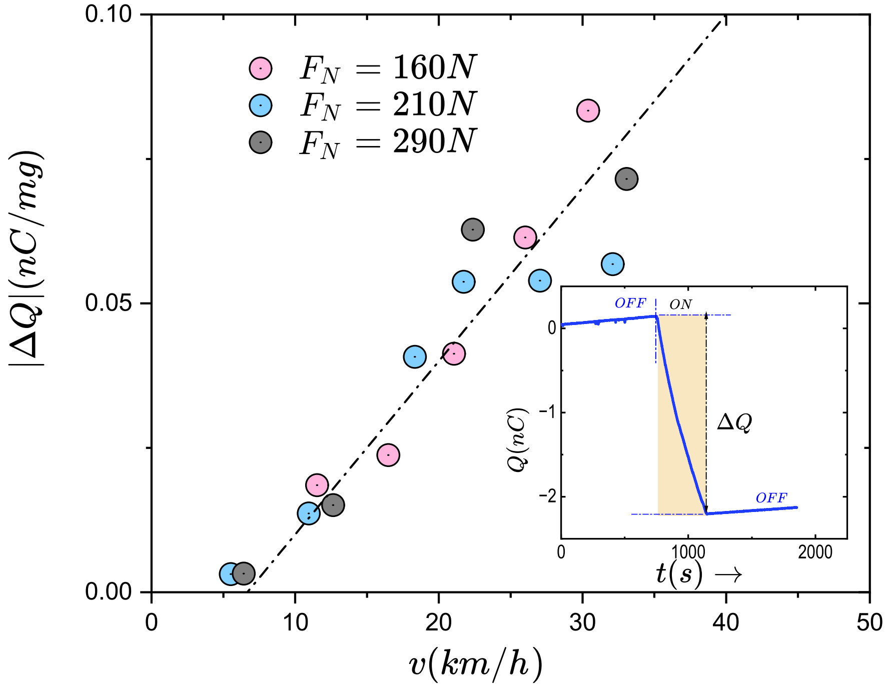

Fig. S8 Variation of the charge $|\Delta Q|$ generated per unit time per unit mass as a function of the velocity v for different values of F_N. The inset shows the variation of the charge recorded by the Keithley 6514 electrometer before, during and after the motion of the tire. The 'ON' and 'OFF' time instances marked on the figure indicates the switching on and off of the power to the tire.

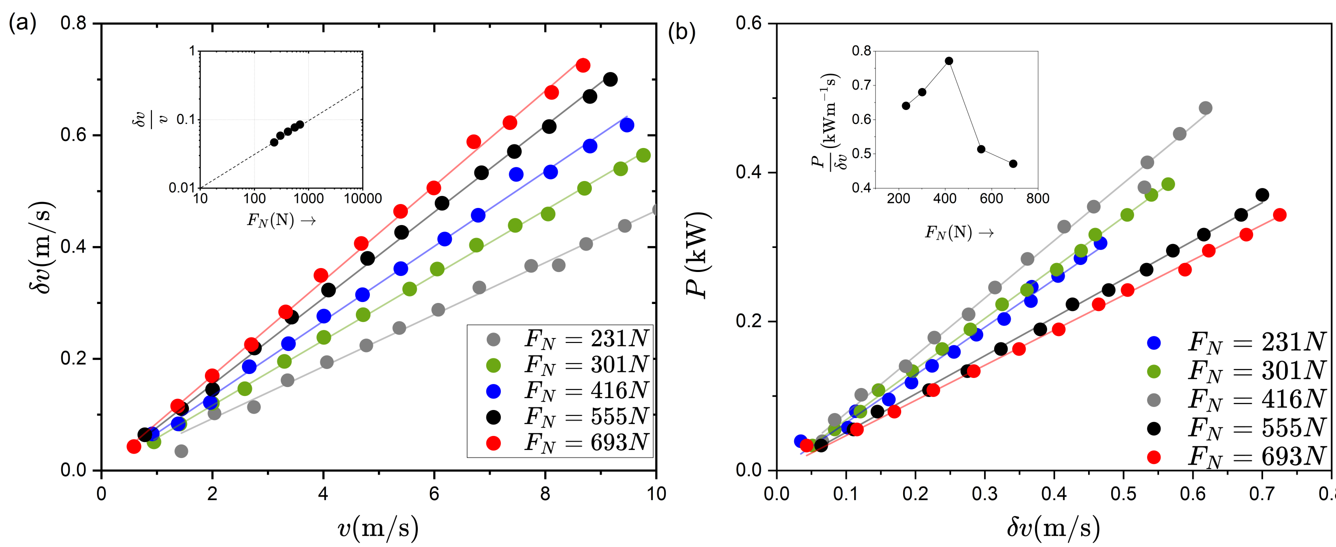

Fig. S9 (a) Shows the linear variation of the slip velocity δv as a function of the velocity v for different values of the normal force F_N. The solid lines represent linear fits to the data. The inset displays the variation of the slope of these fits, $\delta v/v$, as a function of F_N, showing that $\delta v/v \sim \sqrt{F_N}$. (b) Shows the variation in the electric power P consumed by the tire as a function of the slip velocity δv. The solid lines indicate linear fits. The inset reveals the nonmonotonic variation of the slope of these fits, $P/\delta v$, as a function of F_N.